ASCA Observation of the Dipping X-Ray Source X1916-053

Yuan-Kuen Ko[1,2], Koji Mukai[2], Alan P. Smale[2], and Nick E. White

Laboratory for High Energy Astrophysics, NASA/GSFC, Greenbelt, MD 20771

Received _____; accepted _____

accepted to be published in the *Astrophysical Journal*

---

[1]Now at Harvard-Smithsonian Center for Astrophysics, Cambridge, MA. Current address: Code 682.3, NASA/GSFC, Greenbelt, MD 20771. email: kuen@uvcs14.nascom.nasa.gov

[2]Universities Space Research Association

ABSTRACT

We present the results of timing and spectral studies of the dipping X-ray source X1916-053, observed by ASCA during its Performance Verification phase. The detected dipping activity is consistent with previous observations, with a period of 3008s and an intermittent secondary dip observed roughly 0.4 out of phase with the primary dip. The energy spectra of different intensity states are fitted with a power law with partial covering fraction absorption and interstellar absorption. The increase in the hardness ratio during the primary and secondary dips, and the increase in the covering fraction and column density with decreasing X-ray intensity, all imply that the dipping is caused by the photo-absorbing materials which have been suggested to be where the accreted flow hits the outer edge of the disk materials. The spectra at all intensity levels show no apparent evidence for Fe or Ne emission lines. This may be due to the low metal abundance in the accretion flow. Alternatively, the X-ray luminosity of the central source may be too weak to excite emission lines, which are assumed to be produced by X-ray photoionization of the disk materials.

Subject headings: stars: x-ray binaries — x-rays: stars

1. Introduction

X1916-053 was the first X-ray burst source discovered to exhibit periodic dipping behavior, thus providing conclusive evidence that the X-ray source was part of a close binary system (Walter et al. 1982; White & Swank 1982). This dipping phenomenon is assumed to be due to the occultation of the central X-ray source by the accreted flow hitting the outer edge of the accretion disk. This assumption was further supported by the detailed intensity-selected spectral analyses by Smale et al. (1988) and Yoshida et al. (1995). Measurements of the period of the X-ray dipping range from 2985s to 3015s (Walter et al. 1982 on Einstein data; White & Swank 1982 on OSO-8 data; Smale et al. 1988 on EXOSAT data; Smale et al. 1989 on GINGA data; Yoshida et al. 1995 on GINGA data), while the period of optical dipping was observed to be 3027.4 ± 0.4s (Grindlay et al. 1988; Callanan, Grindlay & Cool 1995). The apparent discrepancy between the X-ray and optical periods raises the question of which represents the true orbital period of this binary system and what the mechanism or geometry might be that causes the period difference (see e.g. Grindlay 1991 and Smale et al. 1992). The phase of the dips also jitters. Yoshida et al. (1995) have performed a detailed timing analysis which showed that the phase, duration and depth of the primary dips have a systematic modulation of 5-6 days. Occasional secondary dips were also observed in all these observations, with variable shape and depth. These dips can shift in phase relative to the primary dip.

In this paper, we report the results of the timing and spectral analyses of data from X1916-053 obtained by ASCA during its Performance Verification phase. The same observation has been described by Church et al. (1997). Our analysis proceeded independently from theirs, and includes an analysis of the cycle-to-cycle variability and a search for line emission which does not appear in Church et al. Moreover, we use a different spectral model in our intensity-selected spectral fitting and reach different conclusions,

warranting an independent publication. We present details of the observation and data reduction in Section 2. The timing analysis is discussed in Section 3. Our spectral analysis, and a comparison with other spectral modeling, are discussed in Section 4. In Section 5, we summarize our results.

2. Observation and Data Reduction

X1916-053 was observed by ASCA between 1993 May 2 17:57 UT and May 3 12:40 UT, as part of the Performance Verification phase. The scientific payload of ASCA consists of four co-aligned conical foil telescopes, two with GIS (Gas-scintillation Imaging Spectrograph) detectors and two with CCD-based SIS (Solid-state Imaging Spectrograph) detectors (Tanaka, Inoue & Holt 1994).

Throughout this observation, both GIS detectors were operated in PH mode, recording timing, position and spectral information of each detected photon event. The on-board spread discriminator was off during this observation; while this increases the particle background somewhat, the effect on a bright source such as X1916−053 is believed to be negligible. We apply standard screening criteria, eliminating SAA passages, elevation angle above the Earth's limb of less than 5 degrees, and geomagnetic cut-off rigidity of less than 6. This results in 23 ksec of good data for each GIS instruments. For spectral analysis, the GIS data are further filtered by a circular region centered at the point source with a radius of 24 pixels for GIS2 and 37 pixels for GIS3. For each detector, a background event file is extracted by manually selecting several source-free regions in the detector field.

About 18.5 ksec of usable data were obtained with the SIS detectors in FAST mode, after standard screening (with the same criteria as for GIS data and an additional constraint that the elevation angle above the bright Earth limb be greater than 15 degrees). FAST

mode gives timing information to a precision of 15.625 msec, but only 1 bit of positional information, signifying whether the photon in the inner or outer region of the chip is available in the telemetry. The definition of these regions is programmable, and in this case columns 153 and 267 were the boundaries used. Roughly 11 ksec of the good FAST mode data were taken using the on-board discriminator such that only the inner region data are telemetered. For the remaining 7.5 ksec, both inner and outer region photons were telemetered. We therefore select only the inner region photons for our data analysis for the entire 18.5 ksec.

The lack of position information in FAST mode data prevents us from removing the hot/flickering pixels in the usual manner. On SIS1 the source happened to be inside the address discrimination area, leading to a large number of events due to hot/flickering pixels. Since the photons caused by the hot/flickering pixels are low in energy, we rejected these events by using another filter criterion that selects only photons with energy larger than 0.6 keV (PHA channel >184). We have not subtracted any background from the SIS data, as the background contribution is believed to be negligible for a source as bright as X1916-053.

SIS FAST mode data are further selected based on photon grades, which indicate how many pixels the charge was spread over. We selected FAST mode (1-dimensional) Grade 0, and used the appropriate (imaging mode Grades 0 & 2) response matrix. The telescope effective area was integrated over the inner region of the chip, as defined above. This rectangle-extraction procedure enforced by the lack of position information in FAST mode adds extra uncertainties in the effective area calibration. Since this region is rectangular, while the telescope response has an azimuthal energy dependence, it may affect the determination of the continuum slope. However, the general agreement between GIS and SIS results suggests that this has not been a critical problem. We note that the FAST mode calibration does not affect the search for emission lines once the hot pixels have been

removed.

An additional ~4 ksec of good data were obtained with SIS in the normal imaging mode with either 1-CCD or 4-CCD modes. However, these integrations were too short to be of significant use. Clearly the choice of modes was dictated by the need to verify the operations of the FAST mode rather than to optimize the scientific return. Nevertheless, we believe that these SIS data offer a unique opportunity to search for emission lines in this X-ray source.

3. Timing Analysis

In Figure 1 we plot the χ^2 distribution for the GIS2+GIS3 combined light curve for a range of trial periods. The best period is found to be ~3008s. Since this object was observed for only about 20 ksec, the width of the χ^2 peak is very broad, with FWHM $\sim$ 90 sec. Figure 2 shows the GIS combined (GIS2+GIS3) light curve folded on the 3008s recurrence period of the dips, with phase 0.9 (HJD 2449110.2645) at approximately the minimum of the dip (upper panel) and the number of differential orbital cycles that are included in each phase bin (lower panel). The duration of the dip (defined as the time when the intensity drops to 90% or less of the averaged quiescent level) is about 0.25 phase long. A secondary dip is observed at around phase 0.52. To compare with previous observations, we note that the secondary dips have been reported to occur at phase 0.5 by White & Swank (1982) and Yoshida et al. (1995); at phase 0.4 by Walter et al. (1982); and at either phase 0.5 or 0.6 by Smale et al. (1988) (with the primary dip at phase 0). Figure 3 shows the ASCA data (GIS2+GIS3 combined) during the 22 cycles of the dip period plotted against the folded light curve. Note that the secondary dips occured only during the first $\sim$ 5 cycles of this observation. This is not surprising, given that the recurrence of the secondary dip has been observed by GINGA with an apparent period of 5-6 days (Yoshida et al. 1995). The short

observing time prevents us from making detailed timing analysis, but we can still see from Fig. 3 that the dipping activity changes from cycle to cycle, and that not all cycles exhibit a secondary dip. This indicates the dynamic nature of the occulting materials. Secondary dips have been observed during most observations over the past 10 years, indicating that these dips are formed under the same physical processes with similar underlying physical conditions during this time.

We detected no X-ray bursts during the entire observing period, although there is some possibility that a burst may occur during a high background interval, or the RBM_CONT monitor threshold cut off the high counts from the bursts. Bursts have been observed to recur on timescales as short as 4 hours (Smale et al. 1988; Yoshida 1993) or as long as a day. Since this ASCA observation covered less than 50% of the 22 cycles observed, it is thus not clear whether no burst occurred during this interval or whether the burst(s) merely happened to fall in the data gaps.

Figure 4 shows the GIS combined folded light curves in two different energy ranges ([0.6-1.5 keV] in the top panel, [3-10 keV] in the middle panel) and their hardness ratio ([3-10 keV]/[0.6-1.5 keV] in the bottom panel). We see a clear decrease in softer X-rays during the dip indicating the dip is caused by the existence of photo-absorbing materials in the binary system. Former observations have suggested that these dips are caused by occultation where the accreted flow hits the outer edge of the disk materials. It is interesting to note also that the secondary dip is much more obvious in the low energy range than in the high energy range, showing that the secondary dip, like the primary dip, is caused by the photo-absorbing materials in this binary system.

4. Spectral Analysis

The X-ray energy spectra of X1916-053 in both the quiescent and dipping states have been analyzed by fitting various spectral models (e.g. Smale et al. 1988; Yoshida et al. 1995). It was found that the spectrum that best describes and is consistent with the energy spectra throughout all intensity states is a two-component model: $Af_0(E) + Bf_0(E)exp(-\sigma N_H)$, where one component represents the intrinsic, unabsorbed (quiescent) spectrum (modeled as a power law), and the other is the same spectrum suffering photoelectric absorption corresponding to the dipping activity. The normalizations of both components (A and B) vary independently with the intensity states. The normalization of the unabsorbed component decreases with decreasing source intensity, while the normalization of the absorbed component stays roughly constant but with increasing absorbing column as the source intensity decreases. Church et al. (1997) adopt a specific model consisting of a blackbody component (BB) and a partial covering power law component (PL): $AB_1 * BB + AG * [AB_2 * f + (1 - f)] * PL$, where f is the covering fraction, AG is the galactic absorption, and AB_1 (including galactic absorption) and AB_2 are the absorption for the two components. They found that both the column densities and the covering fraction increase as the source intensity decreases. Both of the above models indicate the existence of photo-absorbing materials responsible for the dipping activity. The formulation of the former model shows no physical relation between the normalizations of the two components, which seems unrealistic if both components respond to the same dipping mechanism. The Church et al. model, on the other hand, suggests there are two intrinsic sources, one (BB) associated with the central compact object suffering direct absorption and the other (PL) associated probably with an accretion disk corona subject to a partially covered absorption. Since the blackbody component comes from the point-like source, it is strongly attenuated once the dipping activity begins (as shown in Church et al. (1997)). Therefore, the existence of this blackbody component seems important in their

spectral analysis only when fitting the non-dip spectra. From the point of view of fitting the spectra at various intensity levels at the same time, it is thus not clear whether this component is really necessary. We thus choose to fit the intensity-selected spectra by one power law with partially covered absorption:

$$I(E) = I_0 E^{-\gamma}(fe^{-N_1\sigma(E)} + (1-f))e^{-N_2\sigma(E)}$$

where γ is the power law index, I_0 is the unabsorbed intensity, f is the covering fraction and $\sigma(E)$ is the cross section of the photoelectric absorption. N_1 and N_2 are the equivalent hydrogen columns in the occulting and interstellar materials, respectively. Note that taking this spectral form presumes one single X-ray source.

We divide the spectra for each detector into four intensity states: 4.0–5.5 c/s; 3.0–4.0 c/s; 1.5–3.0 c/s; and 0.05–1.5 c/s. We denote the four intensity states as HIGH (quiescent), MID-HIGH, MID-LOW and LOW (dip) states, respectively. We use the time filters corresponding to different intensity states for GIS2 and apply them to both GIS2 and GIS3 spectra. The time filters for SIS0 are applied to both SIS0 and SIS1 spectra. The fitting results are shown in Table 1. The values of the reduced χ^2s obtained are 1.124, 1.171, 1.153 and 1.039 for the SIS0, SIS1, GIS2, and GIS3 fits, respectively. The quiescent spectrum shows zero covering, representing the intrinsic spectrum of the X-ray source. The power law index and the equivalent interstellar column can be compared with those of Smale et al. (1988) in which $\gamma = 1.80 \pm 0.02$ and $N_2 = (2.1 \pm 0.5) \times 10^{21}$ cm^{-2}. Since the hard X-ray part of the power law spectrum in Church et al. (1997) is shared by the blackbody component ($kT_b = 2.14$ keV), their power law index is higher ($\gamma = 2.42 \pm 0.21$) than ours and Smale et al. (1988) where only one power law component is adopted. This may also explain the higher interstellar column density they found in their model ($N_H = 4.75 \times 10^{21}$ cm^{-2}). It is apparent that both the covering fraction and the absorbing column density increase with decreasing X-ray intensity. This is consistent with the picture that the dipping activity is

associated with some X-ray photo-absorbing materials which are circulating around the X-ray source. The increase in column density with increasing covering fraction suggests that the occulting materials are thicker or denser when they cover a larger fraction of the source in the line-of-sight.

Figure 5 shows the GIS2 spectra from the four intensity states with the best-fit continuum and their residuals. ASCA has the advantage of having the best energy resolution in the X-ray range among current X-ray instruments. The energy resolution ($\Delta E/E$) at 6 keV is $\sim$ 8% for GIS and $\sim$ 2% for SIS at the time of the observation. However, there is no obvious evidence for lines in the spectra of all four intensity states. We have tried to fit the spectra with either a 6.7 keV (Fe XXV K line) or a 1.017 keV (Ne X Lα) line added. For SIS0 and SIS1 data, adding one such line does not improve the fit. And for GIS2 and GIS3 data, adding one such line only slightly decreases the reduced χ^2 (changes $< 1.5\%$) of the fit. In this case, the equivalent widths of these two lines tend to be smaller for lower intensity states, implying that the lines would be occulted at the same time as the continuum. This is contrary to the accretion disk corona (ADC) model (see e.g. X1822-371, Hellier & Mason 1989) in which the equivalent widths of the X-ray emission lines increase during the partial eclipse of the X-ray source, implying that the line emission lies in a more limited (top) part of the ADC than the bulk of the continuum emission and is not blocked by the companion star during the eclipse phase.

The average X-ray intensity of the quiescent (i.e. 'HIGH') state in the 0.6–10 keV range from GIS2 and GIS3 is 2.9×10^{-10} ergs s^{-1} cm^{-2}. Taking the distance of the source to be 10.8 kpc (Smale et al. 1988), the luminosity of the source is 4×10^{36} ergs s^{-1} (note that this is $\sim$ 50% of that reported by Smale et al. (1988) in the 0.1–15 keV range and $\sim$25% of that reported by White & Swank (1982) in the 0.5–60 keV range). In the spectral model of Church et al. (1997), the 2.14 keV blackbody radiation is assumed to come from the central

compact object. If we assume this blackbody radiation is emitted from the boundary layer on the surface of the neutron star with radius of 10 km, the luminosity of 4×10^{36} ergs s^{-1} would imply a radiating area of only 1.5 % of the neutron star surface. This suggests that the temperature of the blackbody emission derived by Church et al. (1997) may be too high.

Emission lines have been observed in several low-mass X-ray binary systems such as Sco X-1 (White, Peacock, & Taylor 1985) and the ADC source X1822-371 (Hellier & Mason 1989). The lack of such emission in X1916-053 may be attributable to the low metallicity of this system. Smale et al. (1992) found that for X1916-053 the ratio of the measured hydrogen column density to the estimated electron column density, a measure of the metallicity of the absorbing materials, was 0.5 ± 0.1. In this case, we need to assume the absorbing materials causing the dips are the same as those responsible for the X-ray emission. This is reasonable since both come from the accretion of the companion star. Another possibility is that the X-ray luminosity of this system is too weak to excite strong emission lines. If we assume the emission lines are excited by the X-ray photoionization on the accretion disk, the hard X-ray line intensity is roughly dependent on the luminosity of the illuminated X-rays as L_x^2 (Ko & Kallman 1994), which is a strong dependency. It is thus not surprising that no lines are detected, because of the low X-ray luminosity of this source (compared with, e.g., $\sim 10^{38}$ ergs s^{-1} for Sco X-1, White et al. 1986).

5. Summary

The X-ray light curves of X1916-053 show dips with a period of 3008 seconds. No X-ray bursts are detected during this observation. Both the hardness ratios in the primary and secondary dips and the energy spectra of the high/low intensity states support the assumption that the dipping activity results from the occultation of the central X-ray

source by the accreted stream hitting the outer edge of the disk materials. The consistency of the appearance of the occasional secondary dips suggests that the occulting materials, although dynamical in nature, are rather stable in structure and in their underlying physical conditions. No emission lines are detected, probably due to low metal abundance in the absorbing materials, or the low intrinsic X-ray luminosity of the source. Our spectral fitting at various intensity levels shows a good fit using a single power law with partial covering, while the model presented by Church et al. (1997) with two components also showed a good fit to the intensity-selected spectra. Further observations on this object with good statistics and energy resolution may help to investigate which spectral form best represents the spectrum of this system.

REFERENCES

Callanan, P. J., Grindlay, J. E., & Cool, A. M. 1995, PASJ, 47, 153

Church, M. J. et al. 1997, ApJ, 491, 388

Grindlay, J. E., Bailyn, C. D., Cohn, H., Lugger, P. M., Thorstensen, J. R., & Wegner, G. 1988, ApJ, 334, L25

Grindlay, J. E. 1991, in Proc.of the 28th Yamada Conference, Frontiers of X-ray Astronomy, ed. Y. Tanaka & K. Koyama (Tokyo), p69

Hellier, C., & Mason, K. O. 1989, MNRAS, 239, 715

Ko, Y.-K., & T. R. Kallman 1994, ApJ, 431, 273

Smale, A. P., Mason, K. O., White, N. E., & Gottwald, M. 1988, MNRAS, 232, 647

Smale, A. P., Mason, K. O., Williams, O. R., & Watson, M. G. 1989, PASJ, 41, 607

Smale, A. P., Mukai, K., Williams, O. R., Jones, M. H., & Corbet, R. H. 1992, ApJ, 400, 330

Tanaka, Y., Inoue, H. & Holt, S.S. 1994, PASJ, 44, L37

Walter, F, M., Bowyer, S., Mason, K. O., Clarke, J. T., Henry, J. P., Halpern, J., & Grindlay, J. E. 1982, ApJ, 253, L67

White, N. E., Peacock, A., & Taylor, B. G., 1985, ApJ, 296, 475

White, N. E., & Swank, J. H., 1982, ApJ, 253, L61

White N. E. et al. 1986, MNRAS, 218, 129

Yoshida, K., 1993, PhD Dissertation, Kanagawa University, Japan

Yoshida, K., Inoue, H., Mitsuda, K., Dotani, T., & Makino, F., 1995, PASJ, 47, 141

This manuscript was prepared with the AAS LaTeX macros v4.0.

Fig. 1.— The χ^2 distribution for the GIS2+GIS3 combined light curve for a range of trial periods. The best period is found to be 3008s.

Fig. 2.— ASCA light curves of X1916-053, folded on the 3008s recurrence period of the dip, into 100 30s bins. Since there is no long-term ephemeris for this period, the epoch of phase 0.0 is arbitrary. The deepest part of the primary dip is roughly at phase 0.9 (HJD 2449110.2645). Each panel shows 1.5 cycles of data. The upper panel is the GIS-combined light curve. The lower panel shows the number of different orbital cycles that are included in each phase bin.

Fig. 3.— The ASCA observation covered parts of the 22 cycles of the 3008s period. Each panel covers one individual cycle; thin line is the average (identical to Fig.2); the histogram with error bars is the summed count rate from GIS2+GIS3. Note that the secondary dips are limited to the first $\sim$ 5 cycles of this observation.

Fig. 4.— The GIS-combined folded light curves in two different energy ranges: [0.6-1.5 keV] in the top panel, [3-10 keV] in the middle panel. The bottom panel shows the hardness ratio ([3-10 keV]/[0.6-1.5 keV]) of the GIS-combined folded light curves. The ratio increases during the primary and secondary dips.

Fig. 5.— The spectra of GIS2 at four intensity states with the best-fit continuum and their residuals. The four intensity states are labeled, with decreasing X-ray intensity, as HIGH, MID-HIGH, MID-LOW and LOW, respectively.

Table 1. Fitting Parameters of the Continuum Spectra

Detector	Intensity State	γ	N_2[a]	N_1[a]	f
SIS0	HIGH	1.70 ± 0.04	0.33 ± 0.02	$0. \pm 0.$	$0. \pm 0.$
	MID-HIGH	···	···	26.4 ± 19.1	0.160 ± 0.018
	MID-LOW	···	···	31.6 ± 6.80	0.611 ± 0.015
	LOW	···	···	65.5 ± 9.90	0.925 ± 0.006
SIS1	HIGH	1.67 ± 0.03	0.29 ± 0.01	$0. \pm 0.$	$0. \pm 0.$
	MID-HIGH	···	···	23.7 ± 11.1	0.071 ± 0.016
	MID-LOW	···	···	39.1 ± 1.00	0.545 ± 0.013
	LOW	···	···	63.5 ± 7.70	0.929 ± 0.004
GIS2	HIGH	1.85 ± 0.03	0.32 ± 0.02	$0. \pm 0.$	$0. \pm 0.$
	MID-HIGH	···	···	22.6 ± 10.4	0.206 ± 0.013
	MID-LOW	···	···	38.1 ± 18.6	0.461 ± 0.016
	LOW	···	···	74.8 ± 6.56	0.949 ± 0.003
GIS3	HIGH	1.83 ± 0.02	0.31 ± 0.02	$0. \pm 0.$	$0. \pm 0.$
	MID-HIGH	···	···	14.6 ± 12.1	0.062 ± 0.014
	MID-LOW	···	···	9.50 ± 3.30	0.334 ± 0.019
	LOW	···	···	61.8 ± 6.70	0.739 ± 0.006

[a]in unit of 10^{22} cm^{-2}.

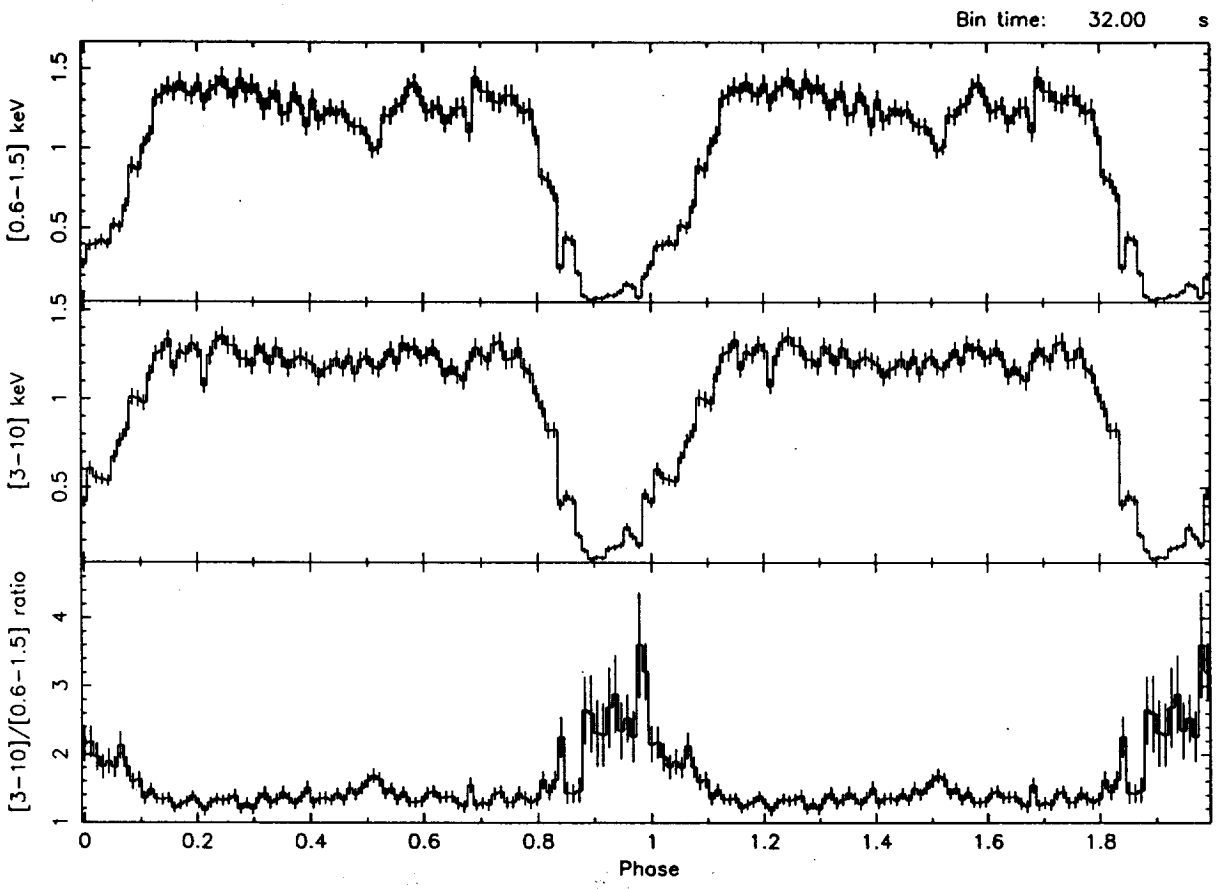
Bin time: 32.00 s
[0.6–1.5] keV
[3–10] keV
[3–10]/[0.6–1.5] ratio
Phase
0
0.2
0.4
0.6
0.8
1
1.2
1.4
1.6
1.8
0.5
1
1.5
2
3
4

Fig. 4

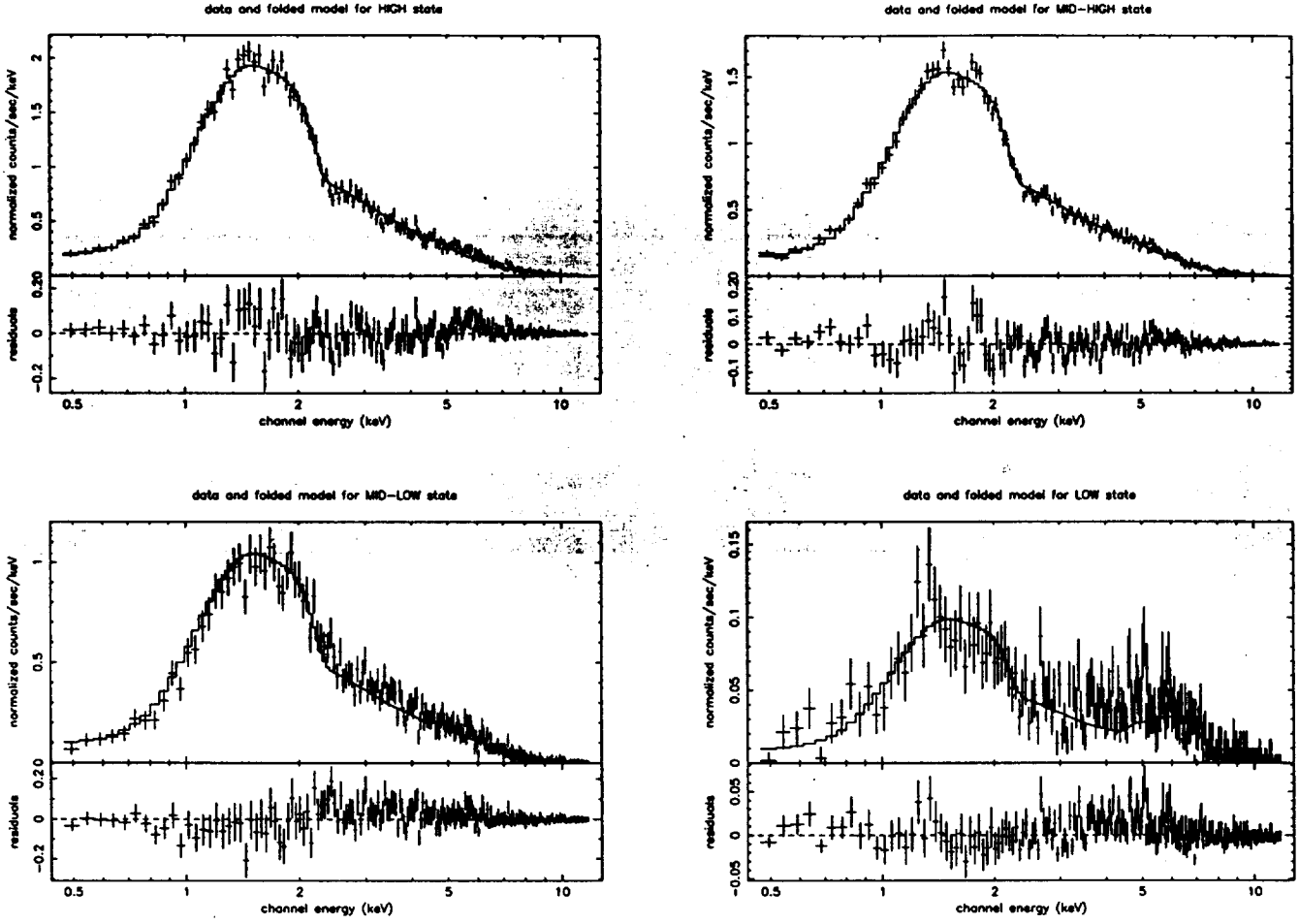
data and folded model for HIGH state
normalized counts/sec/keV
residuals
channel energy (keV)
data and folded model for MID-HIGH state
normalized counts/sec/keV
residuals
channel energy (keV)
data and folded model for MID-LOW state
normalized counts/sec/keV
residuals
channel energy (keV)
data and folded model for LOW state
normalized counts/sec/keV
residuals
channel energy (keV)

Fig. 5